



Effect of Pressure on Hydrogen Enriched Natural Gas Jet Flames in Crossflow

Pankaj Saini¹ · Ianko Chtere¹ · Jhon Pareja¹ · Manfred Aigner¹ · Isaac Boxx¹

Received: 3 February 2020 / Accepted: 15 April 2020 / Published online: 24 May 2020
© The Author(s) 2020

Abstract

The effect of pressure on hydrogen (H_2) enriched natural gas jet flames in crossflow is experimentally investigated here. Simultaneously acquired high speed OH^* chemiluminescence, OH planar laser induced fluorescence (PLIF), and stereoscopic particle image velocimetry are used to study flames at conditions typical of a gas turbine premixer, i.e. at elevated pressure, preheated crossflow, and in confinement. Two different H_2 enrichment levels (40% and 20%, by volume) and pressures (10 bar and 15 bar) were studied here. Flames at the higher H_2 enrichment level were found to be stabilized on the windward side, while the flames at the lower H_2 enrichment were found to be stabilized only on the leeward side. Increased H_2 enrichment was also associated with greater sootiness in the measured region. Jet centerline trajectories showed greater penetration for the higher H_2 enrichment flames, which is in agreement with existing theories on the effect of heat release from a flame on crossflow entrainment. There were no significant changes observed in the mean OH^* chemiluminescence, OH -PLIF, velocity fields, and velocity fluctuation fields with changes in pressure.

Keywords Jet in crossflow · Hydrogen · Laser diagnostics · High pressure

1 Introduction

The work presented here investigates the effects of pressure on hydrogen (H_2) enriched natural gas jet flames in crossflow. Hydrogen is a potential energy carrier candidate for the excess electricity generated from renewable sources, such as wind and solar power. This energy can then be retrieved by mixing it with natural gas and combusting it in gas turbine powerplants. H_2 enrichment of natural gas, however, can alter the mixing and combustion characteristics of a gas turbine. In turbulent diffusion flames, H_2 enrichment of fuels such as NG and LPG has been shown to improve flame stability, reduce flame length, and increase reactivity (Choudhuri and Gollahalli 2003; El-Ghafour et al. 2010). Additionally, H_2 enrichment has been shown to increase NO and CO formation (Choudhuri and

✉ Pankaj Saini
pankaj.saini@dlr.de

¹ Institut für Verbrennungstechnik, Deutsches Zentrum für Luft- und Raumfahrt, Pfaffenwaldring 38-40, Stuttgart, Germany

Gollahalli 2003; El-Ghafour et al. 2010; Kumar and Mishra 2008) and increase soot formation (El-Ghafour et al. 2010; Kumar and Mishra 2008). In non-premixed swirl flames, H₂ enrichment of natural gas was shown to improve flame stability (at lean conditions) but also increased CO and NO_x emissions and increase in soot volume fraction (Cozzi and Coghe 2006). From studies like these, it is apparent that H₂ enrichment of hydrocarbon fuels does change combustion characteristics, and so before its widespread implementation, research at engine relevant conditions is necessary.

The premixer section of a gas turbine combustor is an important component to consider when assessing the effects of changes in the fuel. The mixing characteristics of the air and fuel prior to combustion can affect flame holding, flame stabilization, and emissions, among other things. Many premixers in power generation turbines inject the fuel transversely into the incoming airflow through jets in crossflow (JICF). A JICF typically contains four dominant mixing structures: the shear layer, counter rotating vortex pair (CVP), horseshoe vortices, and wake vortices (Hasselbrink and Mungal 2001a). The combination of these structures is what gives the JICF mixing characteristics that are superior over a jet in coflow or quiescent surrounding. The windward shear layers emanate from the Kelvin–Helmholtz instability and tend to dominate the initial portion of the JICF (Fric and Roshko 1994). In the near field, the shear layer is linked with the formation of the kidney shaped CVP that grows until it dominates the farfield (Kelso et al. 1996). Horseshoe vortices, in line with the crossflow, form in the upstream region of a JICF injected flush from a wall, and wake vortices, that originate from the boundary layer of the wall, form downstream of the jet exit orifice (Karagozian 2010).

The trajectory of a JICF scales with the jet exit diameter (d) and the square root of the jet-to-crossflow momentum flux ratio (r), defined below (Karagozian 2010).

$$r = \sqrt{\frac{\rho_j u_j^2}{\rho_{cf} u_{cf}^2}} \quad (1)$$

In the above equation, u_j and ρ_j are the jet velocity and density, respectively, and u_{cf} and ρ_{cf} are the crossflow velocity and density, respectively. Jet centerline trajectory streamlines are often calculated using the loci of the max velocity. The scaling follows a power law, shown in Eq. 2, where the stream-wise and transverse coordinates (x and y , respectively) are non-dimensionalized by the momentum flux ratio and jet exit diameter (Karagozian 2010).

$$\frac{y}{rd} = A \left(\frac{x}{rd} \right)^B \quad (2)$$

In the above equation, the coefficient A represents the crossflow fluid entrainment and B is a shape constant (Steinberg et al. 2013). Experimental studies on non-reacting JICF have shown constants A and B to lie in the ranges of $1.2 < A < 2.6$ and $0.28 < B < 0.34$, for $r < 25$ (Hasselbrink and Mungal 2001a).

Flame holding and stabilization are important considerations in the design of premixers for gas turbines, as they can impact combustor performance, emissions, and life. Combustion in a jet flame in crossflow (JFICF) can result in altered structure and mixing characteristics, when compared to an equivalent non-reacting JICF. Heat release from combustion in a JICF has been shown to amplify mean velocities and root mean squared (RMS) velocity fluctuations by a factor of 2–3 (Hasselbrink and Mungal 1999). For increasing flux ratios, the flame length of a JFICF has been shown to increase until the flame detaches completely and stabilizes in the form of a lifted flame, where the CVP dominates (Gollahalli et al.

1975). Turbulence in JFICF has been shown to decay faster than in non-reacting JICF (Savas et al. 1997). The heat release from combustion has also been shown to cause jets to penetrate further into the crossflow as it decreases crossflow entrainment (Hasselbrink and Mungal 2001b). The impact of heat release on JICF is thus quite significant.

The addition of H_2 to a JFICF operating on hydrocarbon fuels, such as natural gas, can affect both its the flame and flow field. Compared to methane (the main component of natural gas), H_2 has a much higher flame speed and resistance to strain-induced extinction, and so its addition to the jet is expected to affect both the flame-shape and flame-holding of the JICF. The lower density of H_2 compared to natural gas (by almost eightfold) can reduce the jet to crossflow density ratio. It has been shown that for density ratios less than 0.6–0.7, free jets can become globally unstable (Karagozian 2010). This can result in self-excited shear layer oscillations that would affect the shear layer vortices and consequently the CVP. Since these vortical structures play a key role in the mixing of the fuel and crossflow, the flame and flow field of the JFICF can thus be expected to be altered. There has been work done on H_2 JFICF, but they are either at atmospheric pressures (for instance Steinberg et al. 2013; Brzustowski et al. 1975; Choudhuri and Gollahalli 2000), or at high pressure but in conditions not typical of a single stage gas turbine premixer (e.g. supersonic flows or vitiated flows for reheat combustors). Relatively few studies have been done on H_2 enriched JFICF at conditions found in the premixing duct of a gas turbine engine.

Crossflows encountered by jets in the premixing duct of a gas turbine engine are typically at elevated pressures. Jet trajectories, as mentioned previously, scale with the momentum flux ratio. The influence of pressure is accounted for in this ratio (Eq. 1) through the jet and crossflow densities. The jet trajectory is therefore expected to not be affected significantly by increasing pressure. The flame shape and stabilization, on the other hand, can be expected to change with pressure since flame speed varies with pressure. This change in flame speed may affect the structure and dynamics of the flame at elevated pressure, rendering predictions based on atmospheric conditions inaccurate. It is therefore necessary to study JFICF at elevated pressures in order to understand and predict their behavior in a gas turbine premixer.

In addition to its jet and crossflow conditions, a premixer's geometry must also be considered when emulating JFICFs in such an environment. JICF in premixers are often confined due to the geometry of the premixers, and so it is important to consider these confinement effects. For instance, the opposing wall's boundary layer could affect the mixing characteristics of the jet, and the blockage to the crossflow in the confined channel caused by the jet could change local crossflow velocities, thereby changing the local momentum flux ratio and consequently the jet trajectory. Most of the work done has been on free unconfined jets, jets that are impinging on opposing walls, or jets that don't penetrate into the crossflow (e.g. in film cooling applications). Studies with jets in flow channels, such as (Steinberg et al. 2013; Hasselbrink and Mungal 2001a, b; Kamotani and Greber 1974), have jet length scales (defined here as the product of jet diameter and the momentum flux ratio) much smaller than the width of the flow channel. For instance, in Hasselbrink and Mungal (2001b) the experiment was designed to have the outer jet length scale less than a fifth of wind tunnel width. More experimental data is therefore needed to better understand the effects of confinement for non-impinging jets, as this is important for studying JICF emulating environments in gas turbine premixers.

There is thus a gap in literature for studying H_2 enriched natural gas JFICF in conditions typical of a gas turbine premixer, i.e. under high pressure, preheated, and in close confinement. This work aims to cover that gap through the simultaneous use of hydroxyl radical (OH^*) chemiluminescence (CL), hydroxyl (OH) planar laser induced fluorescence (PLIF),

and stereoscopic particle image velocimetry (SPIV) to get temporally resolved flame and flow field measurements.

2 Experimental Setup

2.1 Test Facility

The experiments for this work were run in a flow facility that was housed in a high pressure rig. The flow facility consists of an optically accessible flow channel (shown in shown in Fig. 1a) mounted inside an optically accessible, high-pressure combustion test rig, and a fuel injector (shown in Fig. 1b). The fuel injector has a 2 mm diameter (d), circular orifice and is mounted flush to the bottom wall of the optically accessible flow channel. A smooth, contoured nozzle is upstream of the orifice of the fuel injector and the nozzle's contour is based on a fifth order polynomial profile design that has been shown previously to produce a uniform, top-hat velocity profile at the exit of the fuel jet (Megerian et al. 2007). A flow conditioning screen is mounted at the inflow of the nozzle. To ensure constant fuel temperature at different crossflow temperatures, the nozzle block is water-cooled.

The flow channel has a rectangular cross-section (measuring 40×60 mm) and consists of three modules. The first two modules are (each) built with four fused silica plates, connected at the corners with metal posts. The third module consists of three fused silica

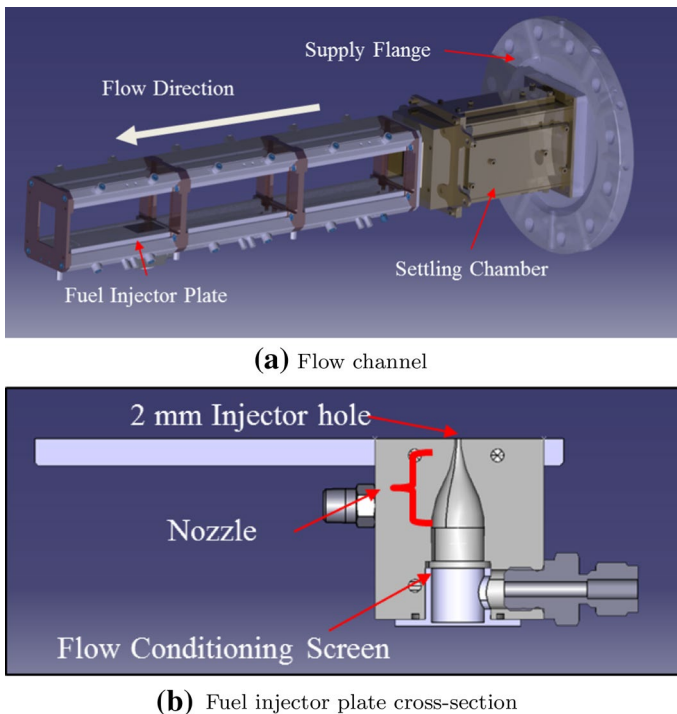


Fig. 1 Sketches of the flow channel and the injector plate used here to study the JFICF

plates and the (stainless steel) fuel injector plate. The fuel injector module was installed in the third (most downstream) module in order to have a stable, well-developed boundary layer on the channel wall upstream of the injector.

A settling chamber, with a flow conditioning screen inside and an inlet for seed air, is placed upstream of the first module. A supply flange is used for the attachment of the flow channel and settling chamber to a high pressure combustion test rig. The flange also provides a pathway for the fuel supply and cooling water for the fuel injector, and thermocouples for the rig and flow channel. The flow channel was mounted in the pressure vessel of the DLR-HIPOT facility. The HIPOT facility has a high pressure, optically accessible combustion vessel that is capable of crossflows at pressures up to 35 bars, thermal loads up to 300 kW, and reactant preheat temperatures of up to 800 K. The large optical accessibility of the rig (through 85×200 mm fused-silica windows) makes it conducive to the laser diagnostic techniques.

2.2 Diagnostics

In this work, high bandwidth, kilohertz (kHz) acquisition-rate laser imaging systems (shown in Fig. 2) were used for the experimental measurements. These include an SPIV system, an OH-PLIF system, and an OH* CL imaging system.

2.2.1 SPIV

The SPIV system used here consists of a pair of highspeed CMOS cameras (Phantom V1212) and a dual-cavity, diode-pumped, solid-state, frequency-doubled Nd:YAG laser (Edgewave, IS200-2-LD). These systems are synchronized through a digital timing and control system (based on the LaVision Davis control software and PTU-X synchronization system). The laser produces pairs of high intensity pulses with energies of up to 9 mJ/ea at a cyclic repetition rate of 10 kHz. Three cylindrical lenses are used to form the SPIV laser sheet of approximately 40 mm (wide) \times 1 mm (thick) at the probe region. TiO_2 particles ($\sim 1 \mu\text{m}$ in size) were used as tracer particles for both the cross-flow and the jet. The cameras have 1280×800 pixel CMOS imaging arrays and are

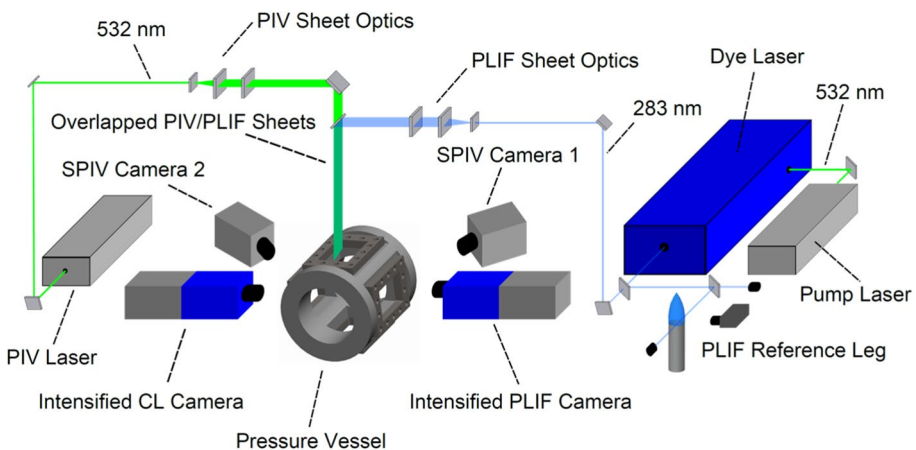


Fig. 2 Sketch of the diagnostics setup

equipped with 72 GB of onboard memory, sufficient for about 4 seconds of recording time at full resolution and 10-kHz acquisition rate. Each camera was equipped with a 200-mm focal-length, $f/4$ macro objective lens (Nikon AF-Micro Nikkor). Background flame luminosity was suppressed through the use of 532-nm-bandpass interference filters. In the present study, the cameras were operated in dual-frame mode at a reduced image size (640×800 pixels), which gives a field of view that spans 48 mm in the axial direction and 60 mm in the transverse direction. To mitigate the image blur associated with off-axis imaging, the objective lenses are mounted on scheinpflug adapters and are adjusted to align the focal plane with the laser sheet.

A commercially available software package (LaVision Davis 8.4.0), using a multi-pass adaptive window offset cross-correlation function, was used to calculate the velocity vectors. The final interrogation window size and overlap were 16×16 pixels and 50% respectively for a spatial resolution of 1.2 mm/vector and vector spacing of 0.6 mm. We note that this resolution is insufficient to accurately capture derivative quantities such as vorticity and shear in the near-field region of the jet, and may also result in spatial smearing of the profiles of mean and fluctuating velocity there. Therefore, we limit quantitative comparisons of mean velocity profiles to further downstream, where the jet and shear layer have expanded to significantly larger scales. Before vector processing, intensity fluctuations in the background, such as ones from reflections, were accounted for through the use of a spatially sliding background intensity subtraction and local particle intensity correction.

2.2.2 OH-PLIF

The OH-PLIF system consists of a frequency-doubled dye laser, a frequency-doubled, Q-switched, diode-pumped solid state Nd:YAG laser to pump the dye laser (Edgewave IS400-2-L, delivering up to 110 W at 532 nm), and an intensified CMOS camera system. The dye laser system (Sirah Credo) produced close to 5 W at 283.9 nm and at a repetition rate of 10 kHz. The OH-PLIF excitation beam is formed into a sheet approximately 40 mm (tall) \times 0.2 mm (thick) using three fused-silica, cylindrical lenses (all anti-reflective coated to maximize transmission), and the OH-PLIF and SPIV laser sheets are overlapped by passing the SPIV sheet through the final OH-PLIF turning mirror.

The dye laser was tuned to excite the (closely spaced) Q1(9) and Q2(8) lines within the $A^2\Sigma^+ - X^2\Pi$ ($v' = 1, v'' = 0$) band. These transitions merge at high pressure due to increased collisional line broadening, which mitigates to some degree fluorescence signal loss due to collisional quenching. The laser wavelength was monitored continuously using a setup consisting of (1) a laminar reference flame, (2) a photomultiplier tube coupled to a 0.1 m monochromator for fluorescence detection, and (3) a digital oscilloscope.

Fluorescence from the A-X (0,0) band was acquired with a CMOS camera (LaVision HSS8), an external two-stage intensifier (LaVision HS-IRO), and a Halle 64-mm focal length, $f/2$ UV lens. Mie scattering from the SPIV seed particles and surface reflections was minimized through the use of a high-transmission ($> 80\%$ at 310 nm) bandpass filter. A 100-ns intensifier gate was used to minimize background luminosity. Spatial variations in imaging system sensitivity were corrected for in post-processing. Acetone vapour was seeded into the measurement plane once a day before taking the measurements and the average of its fluorescence was used to normalize the spatial non-uniformity of the laser sheet.

2.2.3 OH* CL

Another intensified camera was employed here to record OH* CL, a line-of-sight integrated marker for heat release from combustion (Gollahalli et al. 1975). The high-speed CMOS imaging system (LaVision HSS8) was equipped with an external, two-stage intensifier (LaVision HS-IRO) that was fitted with a 45 mm focal length, $f/1.8$ objective (Cerco). A high-transmission, band-pass interference filter was also used. The gate time for the OH* CL signal was 25 μs . Similar to the OH-PLIF measurements, the images here were also corrected for spatial variations in imaging system sensitivity.

2.3 Test Conditions

The experiments were carried out on non-premixed jet flames in crossflow at the four test conditions outlined in Table 1. The conditions correspond to 40% and 20% H₂ enrichment of the natural gas fuel jet, by volume, each at 10 bar and 15 bar. The natural gas used in this consists of approximately 94% CH₄, 4% C₂H₆ and 2% other gases (N₂, CO₂, CO and higher hydrocarbons). Density of the fuel jet was computed based on a mole-weighted sum of the density of hydrogen and natural gas. Viscosity (used to estimate Reynolds number) was calculated based on a mole-weighted sum of hydrogen and methane (the primary component of our natural gas). The fuel, which was unheated, was at 293K.

In order to isolate the influence of H₂ enrichment and pressure, the crossflow temperature and velocity, and the jet to crossflow momentum flux ratio were kept constant for these cases. These crossflow conditions (preheated and at elevated pressure) and momentum flux ratio were set to emulate what one would find in a real gas turbine engine.

3 Results and Discussion

3.1 Instantaneous Fields

Shown in Fig. 3 are the instantaneous plots of simultaneously captured OH* CL, OH-PLIF, and velocity magnitude ($|V|$) fields for the 40% H₂ flame at 10 bar case 1. For all the images presented in this work, the crossflow flows from left to right, and the jet exit orifice has been set as the origin of the coordinate system. The stream-wise and transverse axes are x

Table 1 Test parameters for the four cases

Parameter	Case 1	Case 2	Case 3	Case 4
H ₂ enrichment (by volume)	40%	20%	40%	20%
Crossflow pressure	10 Bar		15 Bar	
Crossflow temperature	465 K			
Crossflow velocity	1.5 m/s			
Jet velocity (V_j)	19.9 m/s	17.5 m/s	19.9 m/s	17.5 m/s
Jet-crossflow velocity ratio	13.26	11.68	13.24	11.66
Jet-crossflow density ratio	0.58	0.74	0.59	0.75
Momentum flux ratio (r)	10.1			
Jet Reynolds number	17,900	19,800	26,900	29,700
Crossflow Reynolds number	22,000		32,800	

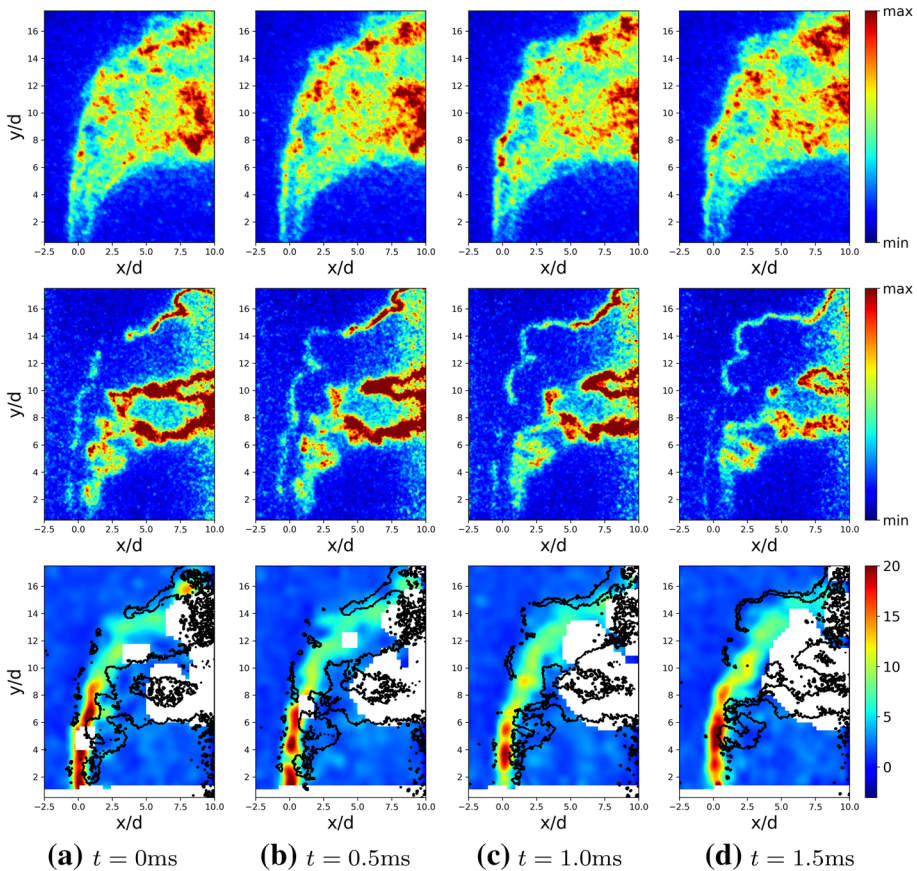


Fig. 3 Instantaneous OH* CL (top row), OH-PLIF (middle row), and $|V|$ fields (bottom row) for the 40% H₂ flame at 10 bar (case 1). The mean $|V|$ fields (in m/s) have overlaid on top the contours of mean binarized OH-PLIF images in black

and y , respectively, and their respective velocities are u and v , respectively. The $|V|$ fields have contours of binarized OH-PLIF images overlaid on top in black. The binarization of the OH-PLIF fields was done using a threshold value that was selected such that the key features of the flames are visible. Contours were calculated from these binarized OH-PLIF images and overlaid on the velocity fields to show the location of the flame with respect to the jet.

The OH* CL fields here show a flame that is attached to the jet orifice and has a flame sheet along the windward side of the jet. This flame sheet appears to follow the growth of the shear layer, given its undulating nature. The OH-PLIF images tell a similar story about the flame. Both the OH* CL and OH-PLIF images show high signal levels on the leeward side of the jet, compared to the windward side. This indicates that there is a more active flame zone on the leeward side since OH* is a marker for heat release in a flame. The OH-PLIF images, on the other hand, indicate the presence of hot (> 1500 K) burned gas along the centerline of the JICF. These observations highlight the strong influence of CVP in the stabilization of the flame and are consistent with previous studies. The contours of

the binarized OH-PLIF images overlaid on the $|V|$ fields show that the flame resides in the periphery of the jet.

The velocity fields in Fig. 3 have some regions with no values (in white) downstream of the jet. This is because these regions had a lot of light scattered from soot particles, which prevented the calculation of velocity from the seed particles. The light scattering from the soot particles can be better seen in the particle images from the PIV measurements. Figure 4 shows images acquired by one of the (bandpass-filtered) PIV cameras simultaneously with those in Fig. 3. In these images, one observes laser scattering both from the PIV particles seeded into flow and from soot formed in the leeward side of the jet. The soot scattering, which appears bright and diffuse in the leeward side of the jet for $x/d > 5$, should not be mistaken for chemiluminescence or broadband flame luminosity, which are effectively eliminated by both the bandpass filter and short integration time of the highspeed camera.

In order to prevent the calculation of erroneous vectors in regions of the flow where scattering from soot (rather than PIV particles) is dominant, images from the PIV cameras were preprocessed with an adaptive mask to remove regions with high soot concentration. This adaptive mask relies upon the fact that, as one can see in Fig. 4, the PIV particles are sufficiently sparse as to appear in the PIV images as discrete particles. In regions where soot scattering is dominant, the soot (which has much smaller particle size, but much higher number density) appears as a more diffuse, high intensity signal in the image. In the adaptive masking algorithm, the ensemble-average of all frames in a measurement run were first subtracted from each individual frame. Next, a (10 pixel) sliding maximum filter was applied (in LaVision Davis 8.4.0). The resulting images have a weak background signal for the seed particles and a strong signal for the soot particles. Finally, a single, user-defined intensity threshold was applied to all images in a measurement run to generate single frame masks. These (binary) masks were then be applied to the original (raw) images to mask out regions where soot scattering is dominant.

Figure 5 shows a sample PIV/soot scattering image and the same image, but with the aforementioned mask applied to it. For regions with low soot luminosity, for instance regions with $x/d < 5$ and $y/d < 8$, the soot luminosity was more diffuse and weaker than the light scattered by the seed particles. In these regions, it was sufficient to use the vector preprocessing tools described in Sect. 2.2.1.

Shown in Fig. 6 are the OH* CL, OH-PLIF, and $|V|$ fields for the 20% H₂ flames at 10 bars pressure (case 2). Similar to Fig. 3, the velocity magnitude fields have overlaid on top the contours of the simultaneously acquired binarized OH-PLIF images. The

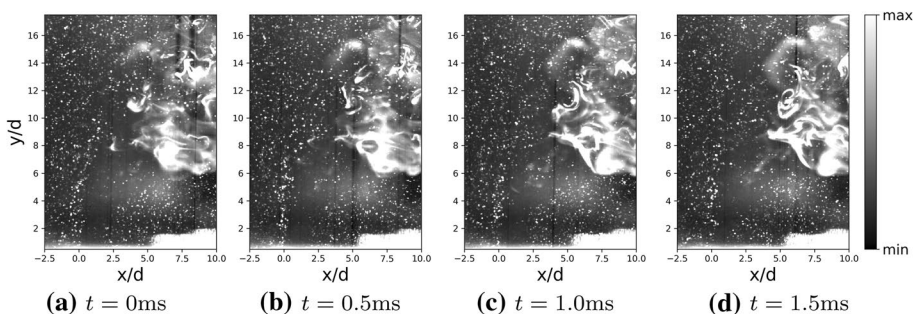


Fig. 4 Images acquired by one of (bandpass filtered) PIV cameras simultaneously with the measurements in Fig. 3, showing significant concentrations of soot particles in the leeward side of the jet

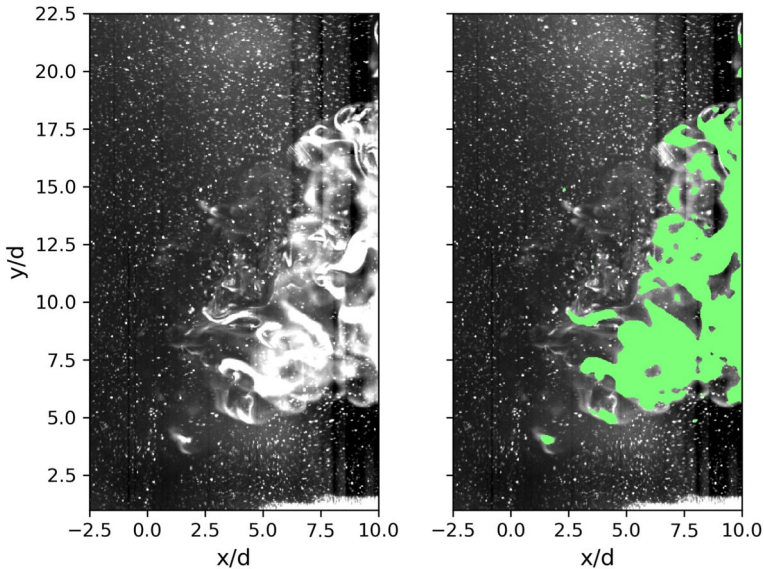


Fig. 5 Sample raw PIV image for case 1, and the same image but with the signal from the soot particles masked (in green)

OH* images indicate the flame is largely extinguished on the windward side of the jet. The flame appears to stabilize downstream from the nozzle in the wake region on the underside of the fuel jet. We note, however, that the flame is not fully lifted, inasmuch as a thin strip of reacting fluid extending all the way to the jet exit is observable in both the OH* and OH-PLIF images. Inspection of the entire image sequence from each run and the ensemble-average images (shown later on in Figs. 8 and 9) indicate the presence of this strip is not intermittent, but rather continuous throughout the measurement run. As the structure is found slightly downstream of $x/d=0$, it is likely the result of a wake behind the jet leading to decreased local shear and possibly mild recirculation. This, combined with the elevated temperature of the crossflow would establish conditions favorable to flame anchoring there. Unfortunately, the spatial resolution of the PIV measurement was insufficient to confirm this hypothesis experimentally. Although the effect of this structure on flame stabilization cannot be proven conclusively in this study, it is reasonable to assume that the heat-release and combustion radicals it generates in the low velocity wake of the jet near-field have a stabilizing effect on the flame downstream.

Comparing Figs. 3 and 6, it is not immediately clear whether the increased local extinction on the windward side of flames with 20% H₂ enrichment results primarily from the effect of hydrogen on the fluid dynamics of the jet in crossflow, or its effect on flame chemistry. A strong argument can be made for it being the effect of H₂ on flame chemistry, given that the laminar flame speed of the fuel increases with H₂-enrichment. Just as with a non-premixed jet flame issuing into a quiescent environment, resistance to flame liftoff scales with the flame speed of the fuel. In addition, despite the 40% H₂-enrichment case having a higher jet-exit velocity (required to maintain a matched momentum flux ratio, while fuel density drops with H₂-enrichment), one observes significantly less windward side-extinction.

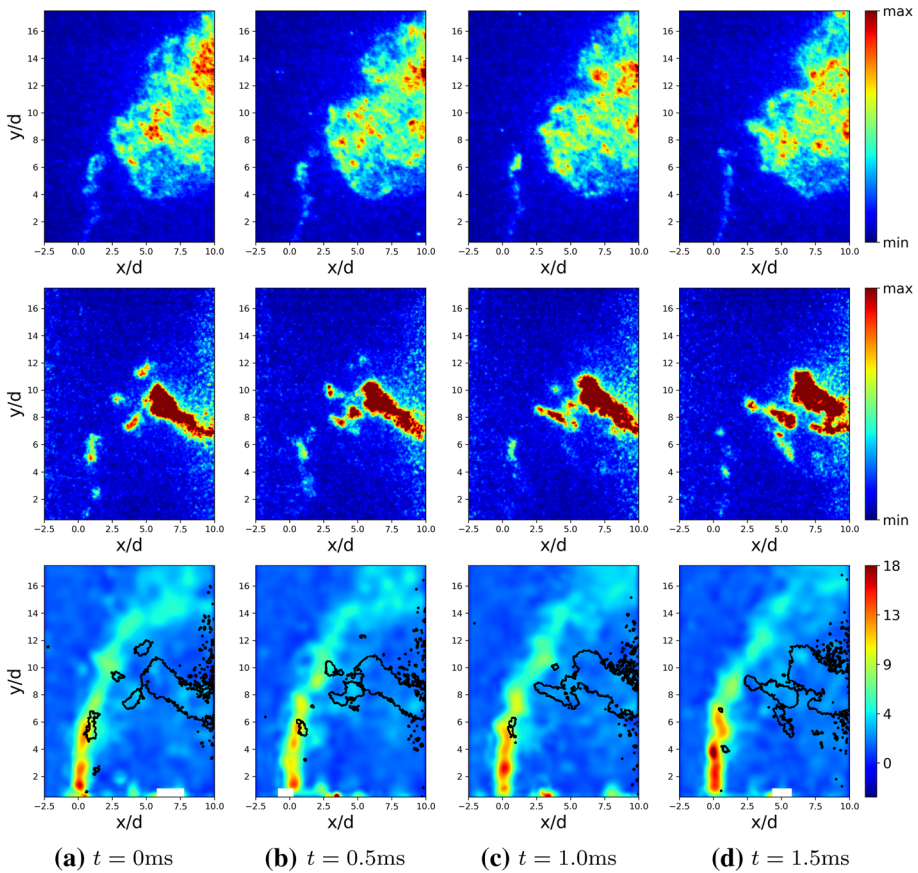


Fig. 6 Instantaneous OH^* CL (top row), OH-PLIF (middle row), and $|v|$ fields (bottom row) for the 20% H_2 flame at 10 bar (case 2). The mean $|v|$ fields (in m/s) have overlaid on top the contours of mean binned OH-PLIF images in black

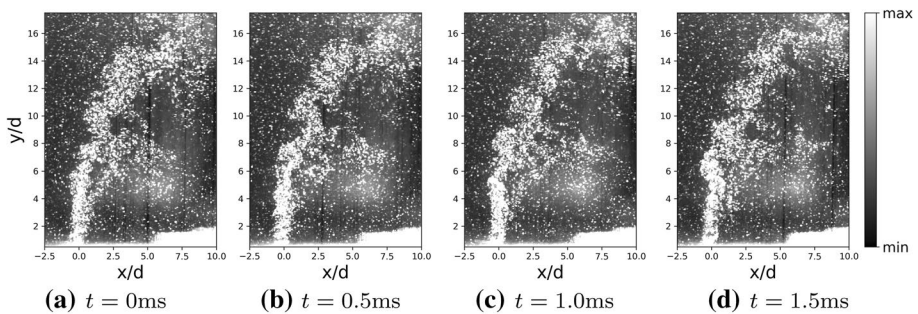


Fig. 7 Images acquired by one of (bandpass filtered) PIV cameras simultaneously with the measurements in Fig. 6. Note the lack of soot in the wake of the jet

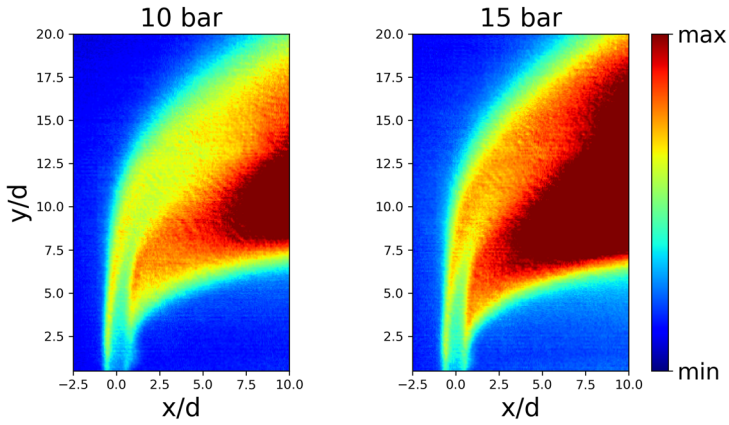
Fig. 8 Mean OH* CL, OH-PLIF, and PIV fields for the 40% H₂ flames at 10 bar and 15 bar (cases 1 and 3, respectively). The mean |V| fields (in m/s) have overlaid on top the contours of mean binarized OH-PLIF images in black and the jet centerline in white

On the other hand, higher H₂-enrichment at constant momentum flux ratio and cross-flow velocity results in a jet with lower jet-exit Reynolds number and lower jet-to-crossflow density ratio. As the turbulence and mixing characteristics of a JICF are affected by both jet-exit Reynolds number and jet-to-crossflow density ratio, the increased local extinction observed for lower H₂-enrichment may have a fluid dynamic explanation. Although a final determination of the cause for increased local extinction on the windward side of the flame is beyond the scope of this paper, it is a clear demonstration of the complex influence of H₂ enrichment on the stabilization of a turbulent flame even a well-understood, canonical flowfield like the jet-in-crossflow.

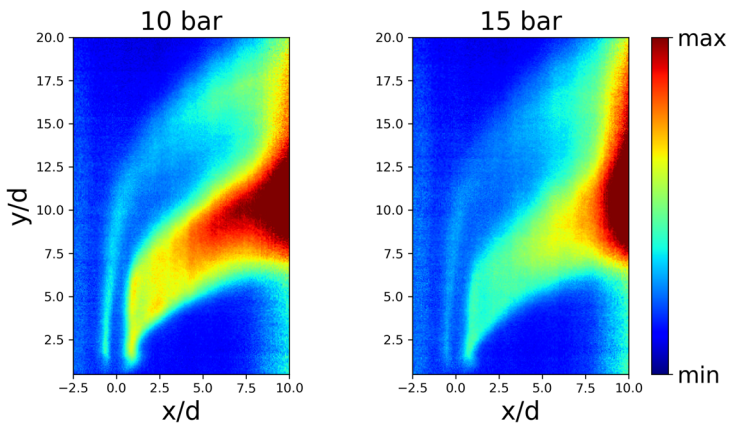
The 20% H₂ flame was found to be not sooty in the measurement region, as shown in its PIV particle images in Fig. 7. This could be due to the presence of a continuous flame sheet along the windward side of the 40% H₂ flame. When the flame sheet envelops the jet on both sides, the oxidizer entrainment is hindered. This results in a more diffusion-like flame, which, at elevated pressures for methane, is sooty by nature. For the cases where there is no flame on the windward side, the unhindered oxidizer entrainment results in a lean, premix flame, which is less sooty due to cooler and more complete combustion. The increase in sooting with increased H₂ enrichment noted here is consistent with previous studies of H₂ enrichment of hydrocarbon fuels in diffusion flames (El-Ghafour et al. 2010; Kumar and Mishra 2008).

3.2 Mean Fields and Turbulence

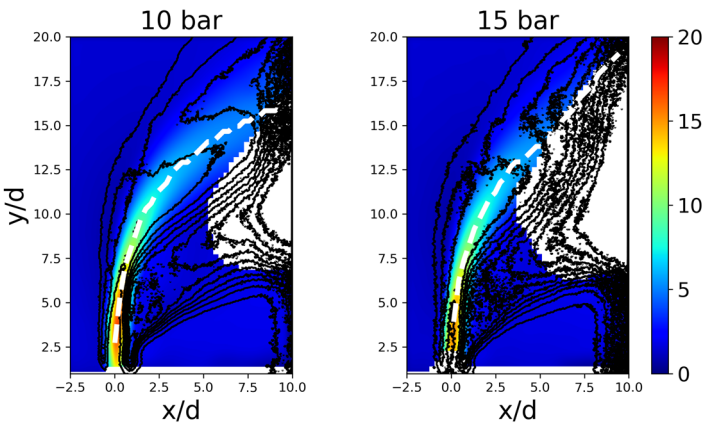
Shown in Fig. 8 are the mean OH* CL, OH-PLIF, and velocity magnitude fields for the 40% H₂ flames at the two pressures: 10 bar and 15 bar. The |V| fields have overlaid on top the contours of the mean of the binarized OH-PLIF images in black and the jet centerline trajectory, defined here as the loci of max centerline velocity magnitude, in white. As mentioned before, due to the sooty nature of the 40% H₂ flame, a mask was applied to ensure that velocities were not calculated using the light scattered by the soot particles. The white regions in the velocity fields correspond to the regions that had a gappiness of over 50%, in time, due to this masking. The mean OH* CL and OH-PLIF fields here show the windward stabilized nature of flame that was noted previously in Fig. 3. The OH-PLIF contours on the velocity fields show the presence of the flame around the periphery of the jet, something that was also noted in the instantaneous fields. With regards to changes caused by pressure, however, there are no significant differences in the mean fields of the two flames. The OH* CL fields show greater signal for the 15 bar case, but this is likely due to an increase in the fuel density at higher pressures, which corresponds to more OH radicals, and therefore a stronger OH* signal. Other than that, the shape of the flame is the same for both pressures. The OH-PLIF mean fields also show the same flame shape at both pressures, but the signal is lower for the higher pressure flame. This is to be expected though as at higher pressures, the signal-to-noise ratio of OH-PLIF measurements has been known to decrease due to reabsorption, laser depletion, and collisional quenching of the excited OH molecules (Strakey et al. 2008). The mean velocity fields also show no significant changes with respect to pressure. From these fields, it appears that the OH PLIF contours span the



(a) Mean OH* CL



(b) Mean OH-PLIF



(c) Mean $|V|$ fields

Fig. 9 Mean OH* CL, OH-PLIF, and PIV fields for the 20% H₂ flames at 10 bar and 15 bar (cases 2 and 4, respectively). The mean $|V|$ fields (in m/s) have overlaid on top the contours of mean binarized OH-PLIF images in black and the jet centerline in white

jet centerline further downstream, which is consistent with previous studies of JFICF (Hasselbrink and Mungal 1998). This could be caused by the transportation of OH radicals by the CVP.

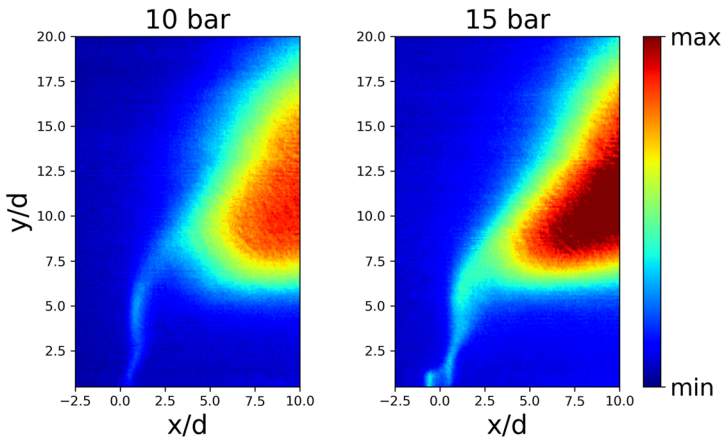
Figure 9 shows the ensemble-averaged OH*, OH-PLIF and PIV measurements for the cases with 20% H₂. Consistent with the instantaneous measurements shown in Fig. 6, the mean OH* chemiluminescence fields show a flame stabilized only on the leeward side of the jet, with a thin strip of active heat-release reaction extending all the way to fuel injection orifice. We note that the flame appears somewhat more lifted in Fig. 9 than implied by the image sequence shown in Fig. 6. This results from the constant axial (upstream and downstream) movement of flame leading edge which causes spatiotemporal smearing of the ensemble-average images. The same effect is observable in the OH-PLIF images. As in Fig. 8, contours of mean OH-PLIF signal are superimposed over the mean velocity field for reference. The contours demonstrate the flame resides most frequently in the low velocity wake on the leeward side of the jet.

Shown in Fig. 10 are the velocity fluctuations of the four flames, with the jet centerline trajectories overlaid on top, in white. From the plots, it can be seen that the velocity fluctuations are high along the centerline, close to the jet exit ($x/d < 2.5$). This is to be expected as the jet velocities in the centerline are the highest, and so their fluctuations will be have a higher absolute value as well. For a given pressure, the higher H₂ enrichment flames have greater velocity fluctuations. This is again possibly due to the higher velocities for these cases, since the momentum flux ratio is being conserved for less dense jets. It does appear that the velocity fluctuations on the leeward side of the jet are higher ($1.5 < x/d < 6$ and $2.5 < y/d < 8$). For a given H₂ enrichment, there only appears to be a slight increase in turbulence fluctuations.

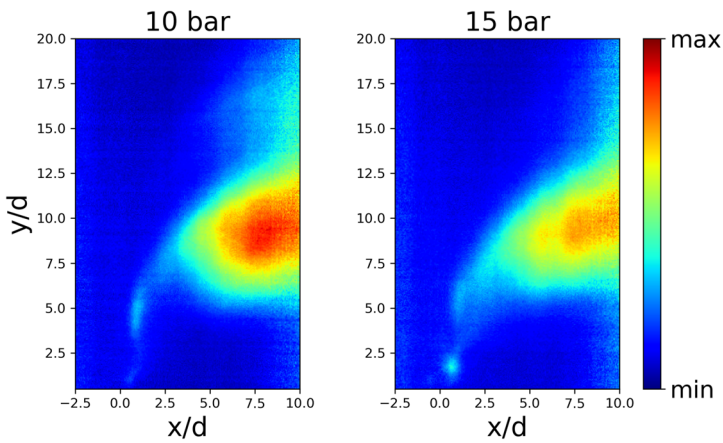
3.3 Centerline Trajectories

The jet centerline was calculated from the loci of the max velocity magnitude of the jet. These loci were determined by finding the location of maximum velocity along a probe line spanning across the jet, at each axial location. The probe lines were set to be perpendicular to the expected jet centerline. The angle of the probe line near the jet orifice was set to 0 degrees (horizontal), since the jet centerline is expected to be near vertical there. The angles at subsequent downstream locations were determined from the scaling of Eq. 2 with an initial guess of the constants A_0 and B_0 . Using least squares regression, the resulting constants for the current iteration i (A_i and B_i) were used as the initial guess for the next iteration, $i + 1$. The probe lines for each iteration were again angled based on the power law scaling using the previous iteration's constants. This was carried on until there was no significant change in the constants between iterations. This ensured that the probe lines were angled perpendicular to the measured jet centerline. The jet centerline trajectory calculations here were done only in the nearfield of the flames ($x/d < 1.5$).

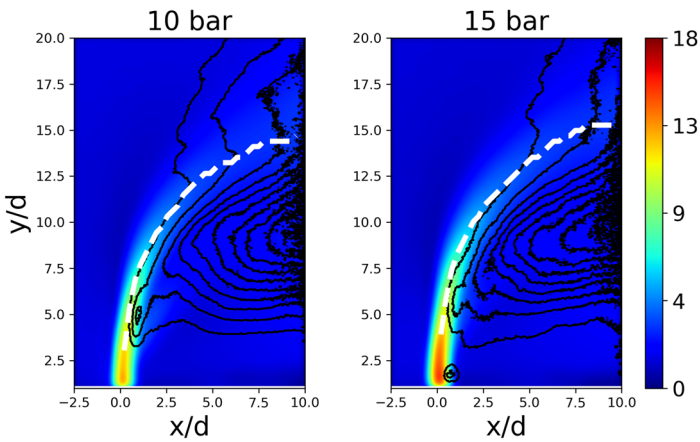
Shown in Fig. 11 are the jet centerline trajectories of the four flames, sorted based on pressure and H₂ enrichment. In Fig. 11a, the trajectory of the 40% H₂ flame shows slightly



(a) Mean OH* CL



(b) Mean OH-PLIF



(c) Mean $|V|$ fields

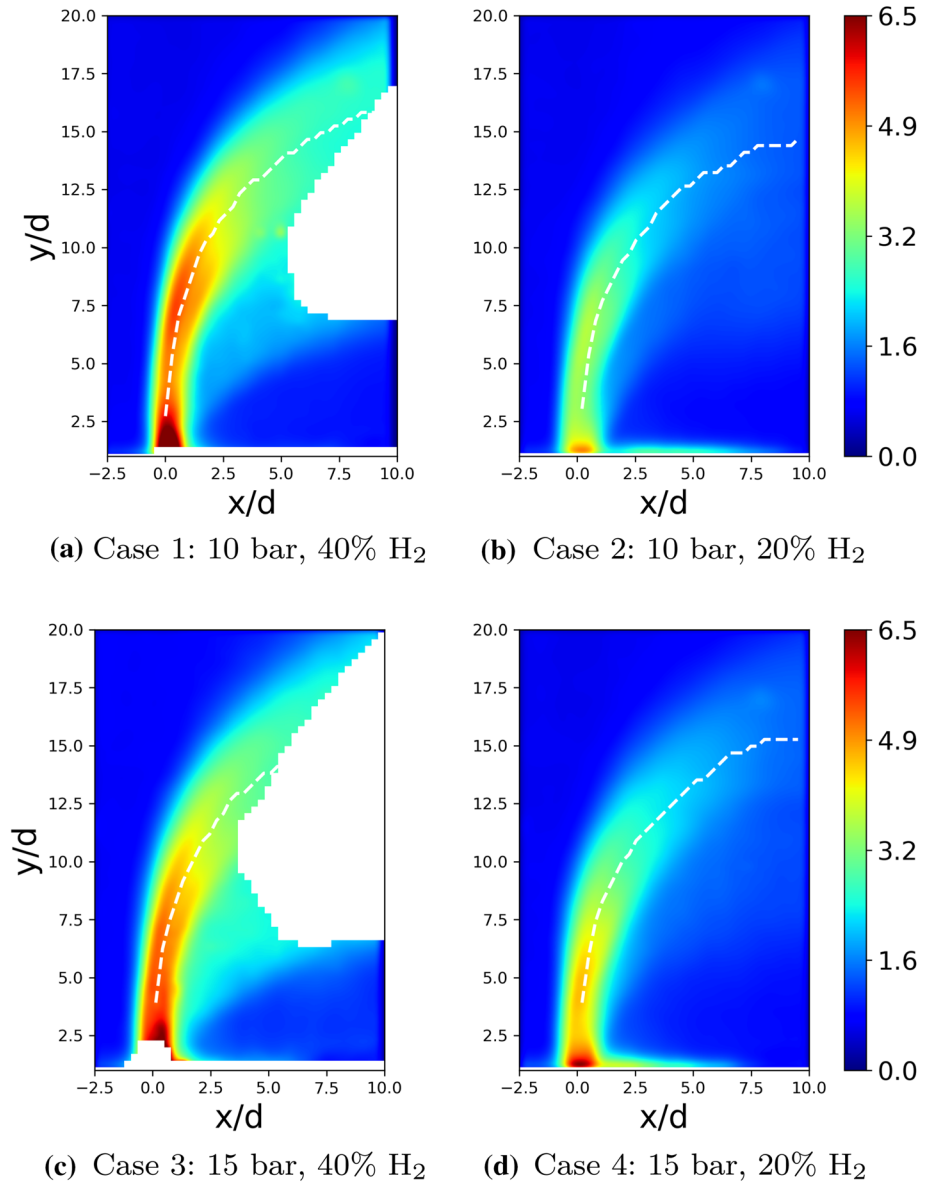


Fig. 10 Turbulence intensity fields for the four flames (in m/s). The jet centerline trajectory is overlaid on top as a dashed white line. The color axis scales are kept constant for all flames

more penetration into the crossflow, when compared to the 20% H₂ case. Given that the 40% H₂ case has a flame on the periphery of the jet, this result makes sense as the heat release from combustion has been shown to increase penetration of jet flames (Hasselbrink and Mungal 1999). This is because the entrainment of the crossflow into the jet decreases, and so the jet is able to penetrate further. At the higher pressure, Fig. 11b, the same trend

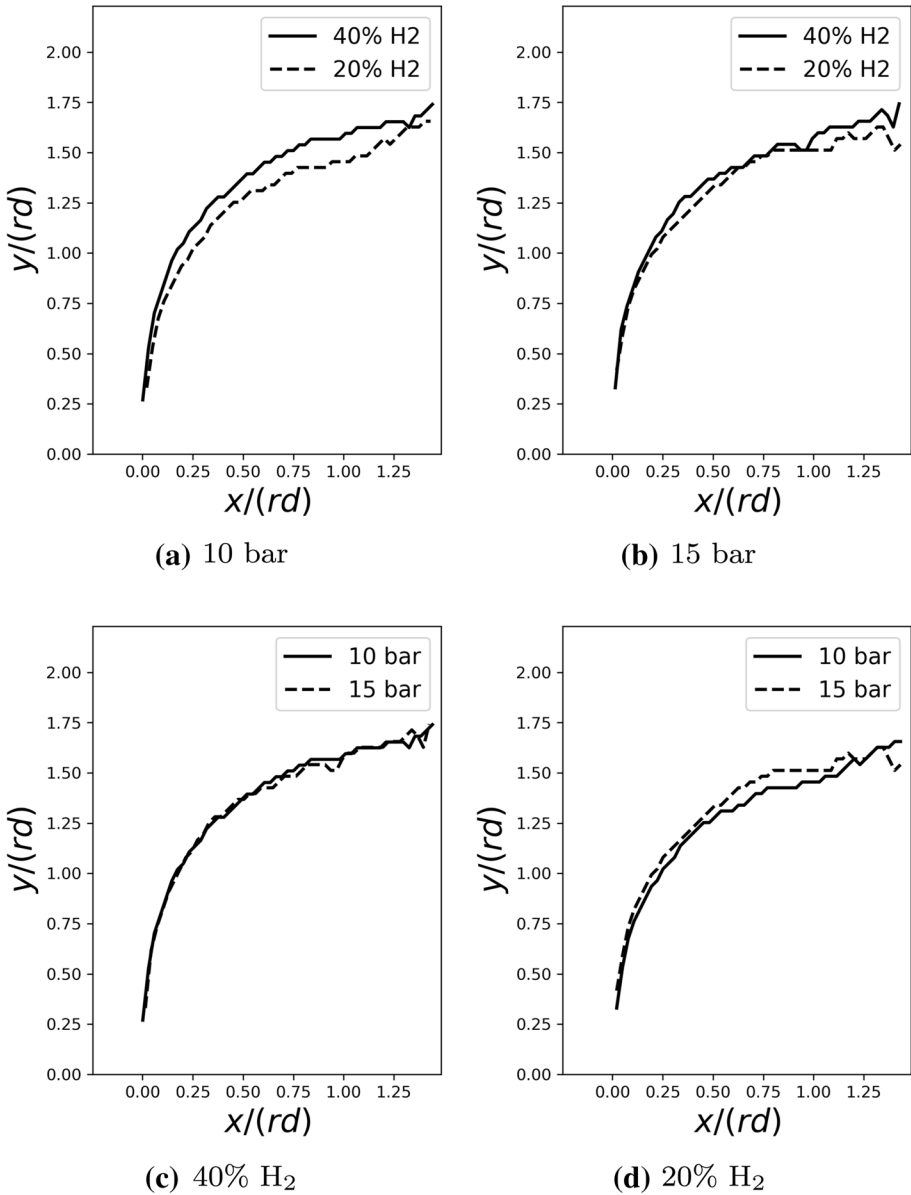


Fig. 11 Jet velocity centerline trajectories for the four flames sorted by pressure (top row) and H₂ enrichment (bottom row)

is noted but the trajectories are slightly closer together. The 40% H₂ flame at this pressure appears to penetrate slightly more than the 20% H₂ flame, but the difference is quite small. The same can be said for the trajectories of the 40% H₂ and 20% H₂ flames at different pressures (Fig. 11c and d, respectively). There appears to be no significant change in the trajectories with pressure, which agrees with theory as pressure changes are reflected in the

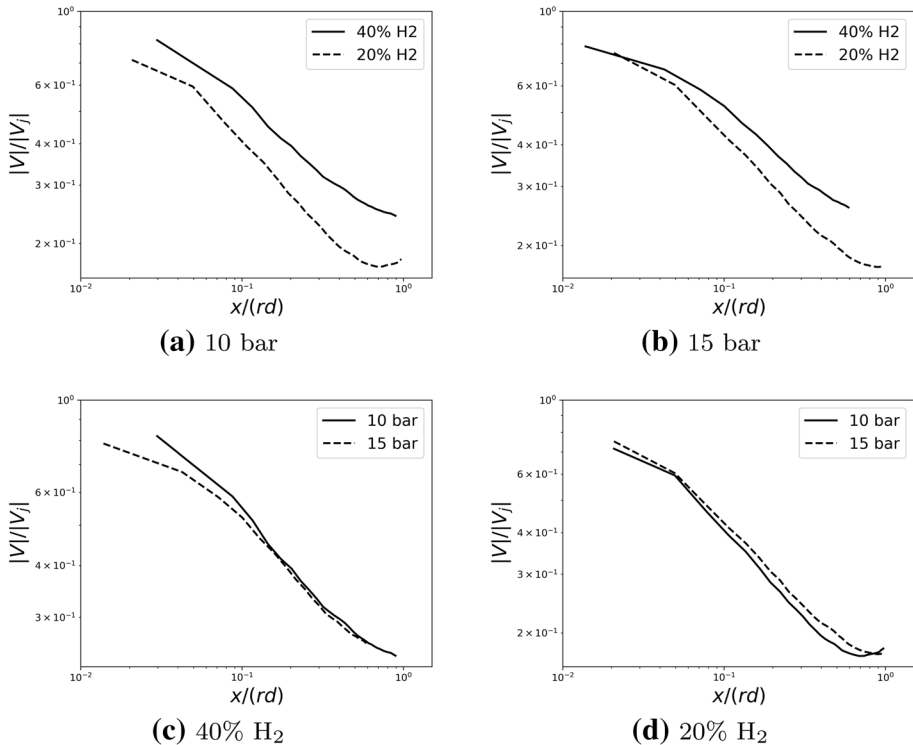


Fig. 12 Jet centerline mean velocities for the four flames sorted by pressure (top row) and H₂ enrichment (bottom row)

jet and crossflow densities, which are accounted for when the momentum flux ratio is preserved. The trajectories here fit the power law scaling (Eq. 2) quite well. The constants for the 40% H₂ flames were 1.6 for *A* at both pressures, and 0.26 and 0.27 for *B* at 10 bar and 15 bar, respectively. The constants for the 20% H₂ flames were 1.49 and 1.55 for *A* and 0.29 and 0.27 for *B* at 10 bar and 15 bar, respectively.

Shown in Fig. 12 are the mean velocities along the jet centerline for the four flames, normalized to the corresponding jet exit velocities from Table 1. From the plots, it is evident that at a given pressure, the 40% H₂ flame has higher velocities relative to its jet exit velocity than the 20% H₂ flame. The decay of the centerline velocities is also higher for the 20% H₂ flames. This discrepancy in the centerline velocities can again be attributed to the difference in the flame stabilization at the two H₂ enrichments. The presence of a flame on the windward side of the 40% H₂ cases possibly results in greater volumetric expansion, which would accelerate the flow. This is similar to the reduction in mean centerline velocity decay caused by combustion in a JFICF when compared to an equivalent non-reacting JICF (Han and Mungal 2001). The plots of the mean centerline velocities of the 40% H₂ flame and 20% H₂ flame at 10 bar and 15 bar (Fig. 12c and d, respectively) show no significant variation caused by pressure. This is again possibly due to the preservation of the momentum flux ratio between the jets, and further shows that the momentum flux ratio is a good non-dimensional parameter to account for changes in pressure for JICF.

4 Conclusion

Hydrogen-enriched natural gas jet flames in crossflow were investigated at two pressures (10 bar and 15 bar) and two H₂ enrichment levels (40% and 20%, by volume). The test conditions were set to emulate conditions typical of a gas turbine premixer, i.e. under high pressure, preheated crossflow, and in close confinement. Instantaneous and mean images of the OH* CL and OH-PLIF showed a mostly lifted flame for the lower H₂ enrichment condition and a nozzle-attached flame for the higher H₂ enrichment condition. The higher enrichment flame was found to be stabilized on the windward side while the lower enrichment flame was found to be attached only on the leeward side.

Mie scattering from soot particles was found to be much higher for the higher H₂ enrichment flame, indicating greater sooting for this case. This is possibly due to the hindering of the entrainment of the crossflow due to the presence of the flame on the periphery of the jet for this case, which would result in a more diffusion like flame compared to the partially premixed flame at the lower H₂ enrichment.

The velocity fields and the simultaneously acquired OH-PLIF contours showed the 40% H₂ flame to reside in the periphery of the jet. OH-PLIF signal spanned the centerline of the jet for both H₂ enrichment levels, a finding that is in line with previous works and could be a result of the transport of hot products by the CVP. Jet centerline trajectories were calculated from the loci of maximum velocities, and they followed existing power scaling law quite well. An increase in H₂ enrichment was found to increase the jet penetration slightly, possibly due to a decrease in crossflow entrainment caused by the presence of a flame on the windward side.

The mean OH* CL, OH-PLIF, velocity fields, and velocity fluctuation fields did not show significant difference in flame shapes or flow field with respect to pressure. Jet centerline trajectories and centerline velocities were also found to show little dependence on pressure. It would therefore appear that, over the range of pressures examined in this study, the effect of pressure on macroscopic flow and flame features is not significant.

Acknowledgement Open Access funding provided by Projekt DEAL. The authors also gratefully acknowledge support from the Natural Sciences and Engineering Research Council of Canada through a doctoral research scholarship.

Funding This project has received funding from the European Research Council (ERC) under the European Union's Horizon 2020 research and innovation programme (Grant Agreement No. 682383).

Compliance with ethical standards

Conflict of interest The authors declare that they have no conflict of interest.

Open Access This article is licensed under a Creative Commons Attribution 4.0 International License, which permits use, sharing, adaptation, distribution and reproduction in any medium or format, as long as you give appropriate credit to the original author(s) and the source, provide a link to the Creative Commons licence, and indicate if changes were made. The images or other third party material in this article are included in the article's Creative Commons licence, unless indicated otherwise in a credit line to the material. If material is not included in the article's Creative Commons licence and your intended use is not permitted by statutory regulation or exceeds the permitted use, you will need to obtain permission directly from the copyright holder. To view a copy of this licence, visit <http://creativecommons.org/licenses/by/4.0/>.

References

- Brzustowski, T., Gollahalli, S., Sullivan, H.: The turbulent hydrogen diffusion flame in a cross-wind. *Combust. Sci. Technol.* **11**(1–2), 29–33 (1975)
- Choudhuri, A.R., Gollahalli, S.: Effects of ambient pressure and burner scaling on the flame geometry and structure of hydrogen jet flames in cross-flow. *Int. J. Hydrog. Energy* **25**(11), 1107–1118 (2000)
- Choudhuri, A.R., Gollahalli, S.: Characteristics of hydrogen–hydrocarbon composite fuel turbulent jet flames. *Int. J. Hydrog. Energy* **28**(4), 445–454 (2003)
- Cozzi, F., Coghe, A.: Behavior of hydrogen-enriched non-premixed swirled natural gas flames. *Int. J. Hydrog. Energy* **31**(6), 669–677 (2006)
- El-Ghafour, S., El-Dein, A., Aref, A.: Combustion characteristics of natural gas-hydrogen hybrid fuel turbulent diffusion flame. *Int. J. Hydrog. Energy* **35**(6), 2556–2565 (2010)
- Fric, T., Roshko, A.: Vortical structure in the wake of a transverse jet. *J. Fluid Mech.* **279**, 1–47 (1994)
- Gollahalli, S., Brzustowski, T., Sullivan, H.: Characteristics of a turbulent propane diffusion flame in a cross-wind. *Trans. Can. Soc. Mech. Eng.* **3**(4), 205–214 (1975)
- Han, D., Mungal, M.: Direct measurement of entrainment in reacting/nonreacting turbulent jets. *Combust. Flame* **124**(3), 370–386 (2001)
- Hasselbrink Jr, E., Mungal, M.: Observations on the stabilization region of lifted non-premixed methane transverse jet flames. In: *Symposium (International) on Combustion*, vol. 27, pp. 1167–1173. Elsevier (1998)
- Hasselbrink Jr, E., Mungal, M.G.: Effects of heat release on jet flames in crossflow. In: *TSEFP Digital Library Online*. Begel House Inc. (1999)
- Hasselbrink, E. F., Mungal, M.: Transverse jets and jet flames. part 1. scaling laws for strong transverse jets. *J. Fluid Mech.* **443**, 1–25 (2001a)
- Hasselbrink, E. F., Mungal, M.: Transverse jets and jet flames. Part 2. Velocity and oh field imaging. *J. Fluid Mech.* **443**, 27–68 (2001b)
- Kamotani, Y., Greber, I.: Experiments on confined turbulent jets in cross flow. In: *6th Fluid and Plasmadynamics Conference*, p. 647 (1974)
- Karagozian, A.R.: Transverse jets and their control. *Prog. Energy Combust. Sci.* **36**(5), 531–553 (2010)
- Kelso, R.M., Lim, T., Perry, A.: An experimental study of round jets in cross-flow. *J. Fluid Mech.* **306**, 111–144 (1996)
- Kumar, P., Mishra, D.: Experimental investigation of laminar lpg-h2 jet diffusion flame. *Int. J. Hydrog. Energy* **33**(1), 225–231 (2008)
- Megerian, S., Davitian, J., Alves, L d B, Karagozian, A.: Transverse-jet shear-layer instabilities. Part 1. Experimental studies. *J. Fluid Mech.* **593**, 93–129 (2007)
- Savas, O., Huang, R., Gollahalli, S.: Structure of the flow field of a nonpremixed gas jet flame in cross-flow. *J. Energy Resour. Technol.* **119**(2), 137–144 (1997)
- Steinberg, A.M., Sadanandan, R., Dem, C., Kutne, P., Meier, W.: Structure and stabilization of hydrogen jet flames in cross-flows. *Proc. Combust. Inst.* **34**(1), 1499–1507 (2013)
- Strakey, P., Woodruff, S., Williams, T., Schefer, R.: Oh-planar fluorescence measurements of pressurized, hydrogen premixed flames in the simval combustor. *AIAA J.* **46**(7), 1604–1613 (2008)